

# Seismic Detection of Oceanic Internal Gravity Waves from Terrestrial Observations

Heather R Shaddock<sup>1</sup>, Emily E Brodsky<sup>1</sup>, Kristen A. Davis<sup>2</sup>, and Steven Richard Ramp<sup>3</sup>

<sup>1</sup>University of California, Santa Cruz

<sup>2</sup>University of California, Irvine

<sup>3</sup>Soliton Oceans Services, LLC

November 23, 2022

## Abstract

Oceanic internal gravity waves propagate along density stratification within the water column and are ubiquitous. They can propagate thousands of kilometers before breaking in shoaling bathymetry and the ensuing turbulent mixing affects coastal processes and climate feedbacks. Despite their importance, internal waves are intrinsically difficult to detect as they result in only minor amplitude deflection of the sea surface; the need for global detection and long time series of internal waves motivates a search for geophysical detection methods. The pressure coupling of a propagating internal wave with the sloping seafloor provides a potential mechanism to generate seismically observable signals. We use data from the South China Sea where exceptional oceanographic and satellite time series are available for comparison to identify internal wave signals in an onshore passive seismic dataset for the first time. We analyze potential seismic signals on broadband seismometers in the context of corroborating oceanographic and satellite data available near Dongsha Atoll in May-June 2019 and find a promising correlation between transient seismic tilt signals and internal wave arrivals and collisions in oceanic and satellite data. It appears that we have successfully detected oceanic internal waves using a terrestrial seismometer. This initial detection suggests that the seismic detection and amplitude determination of oceanic internal waves is possible and can potentially be used to expand the historical record by capitalizing on the existing terrestrial seismic network.

## Hosted file

shaddoxetal\_internalwaves\_si.docx available at <https://authorea.com/users/542872/articles/601085-seismic-detection-of-oceanic-internal-gravity-waves-from-terrestrial-observations>

1  
2

# 1 **Seismic Detection of Oceanic Internal Gravity Waves from Terrestrial Observations**

2

3 **Heather R. Shaddock<sup>1</sup>, Emily E. Brodsky<sup>2</sup>, Kristen A. Davis<sup>3</sup>, and Steven R. Ramp<sup>4</sup>**

4 <sup>1</sup>Department of Earth and Planetary Sciences, University of California, Santa Cruz, Santa Cruz,  
5 CA, USA.

6 <sup>2</sup>Department of Civil and Environmental Engineering and Earth System Science, University of  
7 California, Irvine, Irvine, CA, USA.

8 <sup>3</sup>Soliton Ocean Services, LLC, Falmouth, MA, USA.

9 Corresponding author: Heather R. Shaddock ([hshaddock@ucsc.edu](mailto:hshaddock@ucsc.edu))

## 10 **Key Points:**

- 11 ● Internal waves can generate local tilt potentially observable on coastal broadband  
12 seismometers.
- 13 ● We find promising evidence of the first onshore seismic detection of internal waves.
- 14 ● Seismic coupling preferentially selects waves that collide nearshore.

3  
4  
5**15 Abstract**

16 Oceanic internal gravity waves propagate along density stratification within the water column  
17 and are ubiquitous. They can propagate thousands of kilometers before breaking in shoaling  
18 bathymetry and the ensuing turbulent mixing affects coastal processes and climate feedbacks.  
19 Despite their importance, internal waves are intrinsically difficult to detect as they result in only  
20 minor amplitude deflection of the sea surface; the need for global detection and long time series  
21 of internal waves motivates a search for geophysical detection methods. The pressure coupling of  
22 a propagating internal wave with the sloping seafloor provides a potential mechanism to generate  
23 seismically observable signals. We use data from the South China Sea where exceptional  
24 oceanographic and satellite time series are available for comparison to identify internal wave  
25 signals in an onshore passive seismic dataset for the first time. We analyze potential seismic  
26 signals on broadband seismometers in the context of corroborating oceanographic and satellite  
27 data available near Dongsha Atoll in May-June 2019 and find a promising correlation between  
28 transient seismic tilt signals and internal wave arrivals and collisions in oceanic and satellite  
29 data. It appears that we have successfully detected oceanic internal waves using a terrestrial  
30 seismometer. This initial detection suggests that the seismic detection and amplitude  
31 determination of oceanic internal waves is possible and can potentially be used to expand the  
32 historical record by capitalizing on the existing terrestrial seismic network.

**33 Plain Language Summary**

34 Oceanic internal gravity waves are similar to the more familiar surface gravity waves that travel  
35 along the air-water density boundary at the surface of the ocean, but instead travel along density  
36 boundaries within the water column. Internal waves are important for coastal processes, climate  
37 feedbacks, and general oceanic dynamics and are therefore important to detect and track on a  
38 global scale over time. However, since internal waves are buried within the water column, they  
39 are difficult to detect. Seismology may be able to aid in detecting and measuring the size of  
40 internal waves since a travelling internal wave will deform the underlying seafloor and generate  
41 a local tilt signal that should be observable on coastal broadband seismometers. Here we perform  
42 an initial evaluation of the seismic detectability of internal waves by using Dongsha Atoll in the  
43 South China Sea where we compare an onshore broadband seismometer to internal waves  
44 identified in corroborating oceanic and satellite data. We find correlations between the timing of  
45 transient seismic tilt signals and internal waves identified in oceanic and satellite data. This is  
46 promising evidence of the first onshore seismic detection of internal waves.

6  
7

8  
9

10

**11 Internal waves and expected seismic signals**

12 Oceanic internal gravity waves propagate along density stratification within the water  
13 column (Helfrich and Melville, 2006). These waves are ubiquitous and can propagate thousands  
14 of kilometers before breaking on shoaling bathymetry and the ensuing turbulent mixing affects  
15 coastal processes, climate feedbacks, and marine ecosystems (Wolanski and Deleersnijder, 1998;  
16 Wang et al., 2007; DeCarlo et al., 2015; MacKinnon et al., 2017; Reid et al., 2019). Internal  
17 waves are of further importance for submarine navigation, subsurface structures, hydroacoustics,  
18 and marine organisms, and their critical role in mixing, energy dissipation, and thermohaline  
19 circulation make them one of the most important factors governing oceanic dynamics  
20 (Miropol'sky, 2001; Garrett and Kunze, 2007; Ferrari and Wunsch, 2009; Woodson, 2018).  
21 Internal waves of tidal frequency, called internal tides or baroclinic tides, are generated in  
22 stratified waters when barotropic tidal currents interact with seafloor topography. Internal tides  
23 play a particularly important role in oceanic dynamics because they are generated regularly and  
24 transfer energy from tides to mixing both in the deep ocean and on continental shelves  
25 (Sandstrom and Elliott, 1984; Garrett and Kunze, 2007). Yet, they are not always generated,  
26 even in the same ocean basin. Whether internal tides are generated depends on tide-topography  
27 interactions and ocean stratification (Garrett and Kunze, 2007). Seasonal and climatological  
28 modifications in density stratification can result in dramatic changes in internal tide generation  
29 and propagation. Once generated, internal tides can propagate hundreds of kilometers and then  
30 break up into shorter, higher-frequency nonlinear internal waves (Ray and Mitchum, 1996;  
31 Holloway et al., 1997; Zhao et al., 2004).

32 Despite their importance, internal waves are intrinsically difficult to detect from remote  
33 sensing approaches as they produce only minor amplitude deflection of the sea surface.  
34 Detection of internal waves through sea surface roughness variations visible on satellite images  
35 is possible (Alpers, 1985; Jackson et al., 2013) but limited by cloud cover and temporal  
36 resolution, which is often greater than a tidal period, making it challenging to create a continuous  
37 time series of internal waves. Therefore, short-term (weeks-months) field deployments with in-  
38 situ oceanographic measurements of temperature, pressure and currents at appropriate depths are  
39 used to successfully detect internal waves. However, these deployments only measure  
40 deflections at certain depths and can miss some waves. More importantly, they do not provide  
41 basin-scale spatial coverage or long time series records. The need for global detection and long  
42 time series of internal waves motivates a search for geophysical detection methods.

11

12

2

13  
14

15

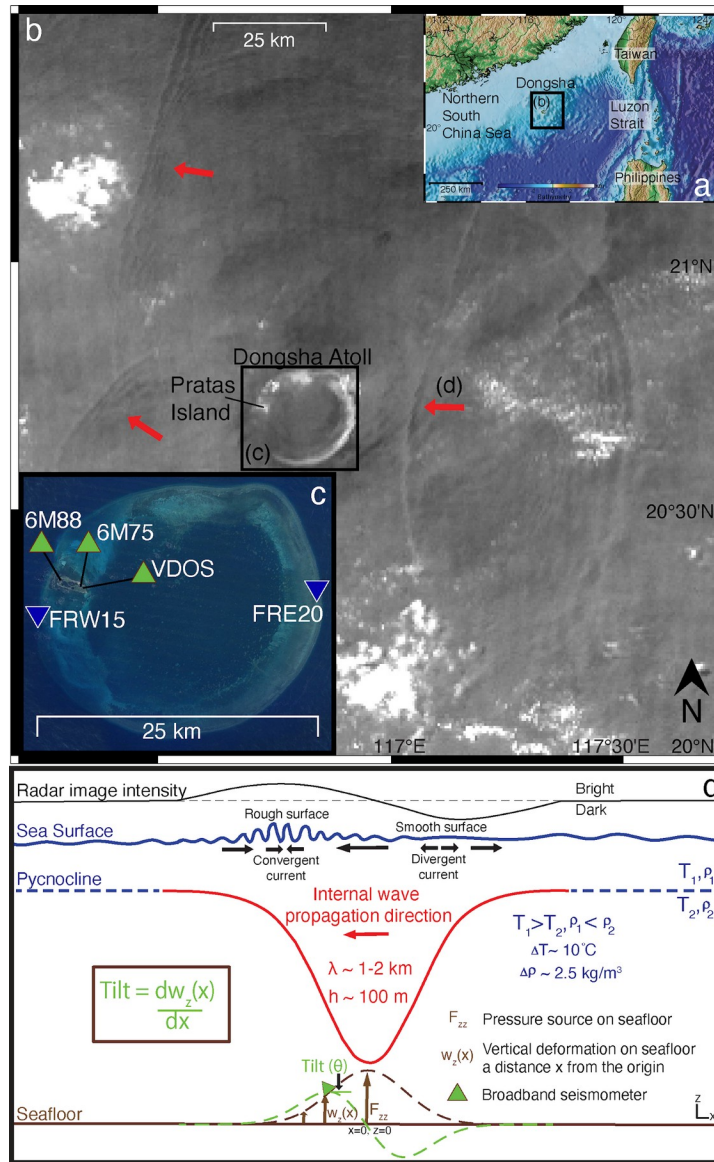
79 The pressure coupling of a propagating internal wave with the seafloor provides a  
80 potential mechanism to generate seismically observable signals. A typical South China Sea  
81 internal solitary wave (i.e., nonlinear dispersive wave) of depression with an amplitude of 100  
82 meters results in a hydrostatic pressure change of approximately 2.5 kPa (Moum and Smyth,  
83 2006), which should generate a near-field tilt on the seafloor around 40 nanoradians (see  
84 Supporting Information section S2 for calculation). Broadband seismometers record rotational  
85 motion/tilt in addition to translational motion because the gravitational force due to a tilt change  
86 results in an acceleration (Wielandt and Forbriger, 1999). A tilt on the order of tens of  
87 nanoradians should be observable at long periods (>100 seconds) on a broadband seismometer  
88 (Ackerley, 2014), and would be expected as internal waves approach and pass a seismic station  
89 (Figure 1d). Since the seafloor is elastic, a broadband seismometer can also detect a tilt signal  
90 from a wave not passing directly over the instrument if the wave is within a distance roughly  
91 equal to the finite source length (i.e., the wavelength of the wave). This is a simplified view that  
92 provides a minimum bound on the potentially observable seismic signals. As will be discussed  
93 later in this study, there are additional potential mechanisms for seismic wave generation by  
94 internal waves. For instance, depending on the environment, the dynamic pressure change on the  
95 seafloor from breaking or interacting internal waves may also result in a seismically observable  
96 signal (Moum and Smyth, 2006). In principle, seismology should be able to fill in the  
97 observational gap and provide long-term time series of internal waves. If successful, the  
98 technique could potentially provide information about the historic record since the mid-20th  
99 century and track the potential reaction of internal waves to climate change.

100 Here we perform an initial evaluation of the seismic detectability of internal waves by  
101 analyzing potential seismic signals in the context of corroborating data. This pilot project is  
102 possible because of exceptional in situ data available from Dongsha Atoll in the South China  
103 Sea. On Pratas Island at the western side of Dongsha Atoll (Figure 1b, c) a permanent seismic  
104 station (VDOS) and two temporary seismometers (May-June 2019) provide broadband seismic  
105 data. A temporary oceanographic deployment (May-June 2019) and available satellite data  
106 provide constraints on the arrival times of internal waves at Dongsha Atoll. We find a promising  
107 correlation between transient seismic tilt signals and internal wave arrival times in oceanic and  
108 satellite data, potentially leading the way to utilizing seismology for both the detection and  
109 amplitude determination of internal waves.

16

17

18  
19  
20



110

111 **Figure 1.** Map of the study area and schematic of a propagating internal solitary wave in the  
 112 South China Sea. (a) Bathymetric map of the northern South China Sea. (b) Himawari-8 standard  
 113 red channel image of sea surface reflections on May 15, 2019 05:30 UTC near Dongsha Atoll.  
 114 Westward propagating internal waves are indicated by red arrows, including an incoming  
 115 internal solitary wave from the Luzon Strait 500 km east of Dongsha Atoll, and the northern and  
 116 southern arms of internal wave trains that are interacting and reforming west of Dongsha Atoll.  
 117 (c) Zoom in of Dongsha Atoll. Oceanic temperature sensors shown as blue inverted triangles and  
 118 land broadband seismometers on Pratas Island are shown as green triangles. (d) Cartoon of a  
 119 typical internal solitary wave in the South China Sea and the resulting (exaggerated) transient  
 120 deformation (dashed brown curve), near-field tilting (dashed green curve) of the underlying  
 121 seafloor (brown line), sea surface roughness (solid blue line) and radar image intensity (black  
 122 line).

21  
22

23  
24

25

## 123 **2 Dongsha Atoll and the South China Sea**

124 The largest amplitude ( $>100$  m) internal solitary waves (i.e., nonlinear dispersive waves)  
125 in the world have been observed in the South China Sea. Depending on the stratification, internal  
126 solitary waves can propagate as waves of depression or elevation. The pycnocline in the South  
127 China Sea is  $< 100$  m, but the basin is deep (up to 5000 m depth). This type of stratification is  
128 expected to generate waves of depression as have been observed in the northern South China Sea  
129 (Ramp et al., 2010; Simmons et al., 2011; Fu et al., 2012). Large diurnal and semidiurnal  
130 barotropic tidal currents flow roughly east-west over two north-south trending ridges in the  
131 Luzon Strait (Figure 1a), generating strong internal tides that propagate westward into the South  
132 China Sea in a narrow beam, steepening into internal solitary waves of depression (Duda et al.,  
133 2004; Ramp et al., 2004; Lien et al., 2005; Alford et al., 2015). Internal solitary waves, typically  
134 two per day, are generated at peak tidal velocities and their amplitude is modulated on a  
135 fortnightly cycle, with the largest amplitude waves generated at peak spring tide when the  
136 barotropic tidal forcing is greatest (Duda et al., 2004; Ramp et al., 2004; Lien et al., 2005).  
137 Internal waves occur regularly in the South China Sea between March and November and  
138 occasionally from December to February (Simmons et al., 2011). Ocean stratification is strongest  
139 in autumn and weakest in winter; since the generation of internal tides is dependent on  
140 stratification, this is likely the cause for the significant decrease in internal wave generation in  
141 the winter.

142 Dongsha Atoll is a 28 km diameter coral reef at the edge of the continental shelf in the  
143 northern South China Sea located approximately 500 km west of the Luzon Strait (Figure 1). It  
144 takes roughly 50 hours for internal waves generated in the Luzon Strait to arrive at Dongsha  
145 Atoll (Davis et al., 2020). Both modeling and observations of internal solitary waves as they  
146 propagate upslope at Dongsha Atoll suggests that an incident symmetric depression wave  
147 collapses into a packet of elevation waves during shoaling (Fu et al., 2012; Rogers et al., 2019).  
148 These wave trains break into northern and southern arms that refract around the atoll, eventually  
149 colliding and then reforming west of Dongsha Atoll (Figure 1b).

## 150 **3 Data and Methods**

151 In order to identify internal wave signals in passive seismic data, we compare seismic  
152 observations from one permanent and two temporary seismic stations onshore of Pratas Island to  
153 established internal wave signals in satellite and oceanographic data during a temporary  
154 deployment in mid-May to mid-June 2019.

### 155 **3.1 Satellite and Oceanographic data**

156 Alternating convergence and divergence zones above internal waves result in sea surface  
157 roughness changes that are visible from sun glint on satellite images (Alpers, 1985; Jackson et  
158 al., 2013). We use the 10-minute temporal and 500-meter spatial resolution standard red channel  
159 ( $0.64 \mu\text{m}$  wavelength) data of the Himawari-8 geostationary meteorological satellite operated by  
160 the Japan Meteorological Agency (JMA) to identify internal waves based on sea surface  
161 roughness changes for comparison to seismic observations (Figure 1b, d). With these images we  
162 can identify internal waves near Dongsha Atoll during daylight hours when there is little cloud  
163 cover.

26  
27

28  
29

30

164 Shoreward of the 100-meter isobath on Dongsha Atoll, internal solitary waves have  
165 transformed into packets of elevation waves (Fu et al, 2012; Davis et al, 2020). This is recorded  
166 as a sudden drop in water temperature measurements, approximately 4-8°C within several  
167 minutes, and is a well-established indicator of the passage of internal waves (Davis et al., 2020).  
168 We can therefore use the arrival times of internal waves from in-situ oceanographic temperature  
169 measurements to compare to a potential internal wave signal in coastal seismic data. To this end,  
170 we use 1-10 second sampling rate oceanic temperature measurements in the water column and on  
171 the ocean bottom during a temporary deployment in May/June 2019 around the fore reef of  
172 Dongsha Atoll (Figure 1c). We utilize a 20-meter mooring on the eastern side of Dongsha Atoll  
173 (FRE20) at 19 meters depth from May 13-June 11, 2019 and an ocean bottom temperature sensor  
174 at approximately 16.8 meters depth on the western side of Dongsha Atoll (FRW15) roughly 4.5  
175 km southwest of a permanent seismic station onshore of Pratas Island from May 19-June 6,  
176 2019. These shallow temperature sensors are located at depths where the large internal waves  
177 have already broken down slope into nonlinear elevation waves or internal bores, but they will  
178 still capture an internal wave signal, albeit a more complex and high-frequency one and lagged  
179 from the arrival time of the wave in deeper water as the wave decelerates in shallow water  
180 (Davis et al., 2020). Further, these point measurements may miss internal wave arrivals  
181 depending on stratification and reflection properties of the internal waves.

182 To help guide the detection of internal waves arriving from the Luzon Strait on these two  
183 shallow temperature sensors we rely on the timing of internal wave detections from two deeper  
184 (300 m and 500 m depth) moorings 6-9 km east of Dongsha Atoll before internal solitary waves  
185 of depression have interacted much with the bottom or transformed into packets of elevation  
186 waves. In particular, we use the wave arrival times at the 300 m mooring, wave velocities  
187 calculated between the 500 and 300 m moorings, and the distances from the 300 m mooring to  
188 the eastern (FRE20; 6.7 km) and western (FRW15; 30.9 km) sensors to estimate the wave arrival  
189 times at these shallow sensors. However, these are used as rough time estimates only since they  
190 are based on the wave velocity between the 500 m and 300 m moorings, which on average was  
191 1.8 m/s during the deployment, and wave velocities can decrease below 0.5 m/s in shallow water  
192 (Fu et al., 2012; Davis et al., 2020). Variations in wave velocity create uncertainty in arrival  
193 times at the shallow temperature sensors. For example, a wave with a phase speed of 2 m/s  
194 would propagate around the 28 km diameter atoll in approximately 3.9 hours, while a wave with  
195 a phase speed of 1 m/s would propagate the same distance in 7.8 hours. It is therefore difficult to  
196 predict the exact arrival time of waves at the shallow sensors without measurements of the wave  
197 velocities in shallow water.

### 198 3.2 Seismic data

199 For seismic data we primarily use the three-component broadband seismometer VDOS  
200 operated by the Broadband Array in Taiwan for Seismology (BATS) network located onshore of  
201 Pratas Island on the west side of Dongsha Atoll (Figure 1c). This Trillium 120-second posthole  
202 instrument is deployed at 2.7 meters depth and has a 100-Hz sampling rate. We additionally  
203 deployed two temporary broadband seismometers (6M88 and 6M75 on Figure 1c) on Pratas  
204 Island from May 11 - June 4, 2019. The signal-to-noise ratio for these two instruments is lower  
205 than for VDOS; these stations are primarily used for confirmation of signals observed on VDOS.

31  
32

33  
34

35

206 Internal solitary waves of depression in the South China Sea propagate with velocities of  
207 2-3.5 m/s (depending on water depth) and wavelengths of 1-2 km. Therefore, in the deep basin,  
208 the period of these waves is about 285-1000 seconds. As the waves shoal at Dongsha Atoll, they  
209 slow and break up into a packet of shorter period (200-850 s) elevation waves (Fu et al, 2012;  
210 Davis et al, 2020). Therefore, it is reasonable to look for a long period tilt signal of passing  
211 internal waves on the horizontal components of VDOS. We anticipate a seismically observable  
212 tilt signal within roughly 10 km of the source based on the 1-2 wavelength of these waves. We  
213 first decimate the 100-Hz VDOS raw seismic data to 1 Hz by downsampling by a factor of 10  
214 twice, each time applying a low-pass filter. We then apply an acausal (two-pass) 400-second  
215 low-pass filter to the decimated seismic data. We do not remove the instrument response when  
216 initially identifying small, transient tilt signals in VDOS that are potentially from internal wave  
217 activity to prevent identifying deconvolution artifacts as signals. The raw seismic data is in  
218 counts, which on VDOS is proportional to velocity at periods below 120 seconds.

219 There is a diurnal seismic tilt signal on the horizontal components of VDOS (Figure 2),  
220 6M75 and 6M88 during daylight hours (22:00 - 10:00 UTC; 6 am - 6 pm local time). This  
221 presents a challenge in differentiating between other diurnal tilt-generating signals such as tidally  
222 modulated internal waves; the source of this diurnal tilt “noise” is therefore important. Daily  
223 temperature fluctuations can cause a change in instrument sensitivity at long periods. Daily  
224 temperature fluctuations for the tropical climate on Pratas Island are  $\sim 5^{\circ}\text{C}$  (Figure S1). For this  
225 temperature change, the instrument sensitivity change is about 0.04% (Anthony et al., 2018). The  
226 diurnal tilt changes are greater than this sensitivity change. In addition, the Trillium 120-second  
227 posthole sensor is buried at 2.7 m depth, below the depth where surface temperature variations  
228 are strongest. It is therefore unlikely that the diurnal tilt signal is from instrumental changes in  
229 sensitivity with temperature. It is more likely that the diurnal signal is from Pratas Island tilting  
230 as a result of diurnal temperature fluctuations as has been observed on other islands (Bilham and  
231 Beavan, 1979; Arnosó et al., 2001; Ekström et al., 2006). The amplitude variations of the seismic  
232 signal do not correlate with the amplitude of land temperature measurements recorded on the  
233 island (Figure S1). In particular, when daily temperature fluctuations on Pratas Island are largest  
234 (May 16 - May 21), the diurnal tilt signal in the seismic recordings is lowest. However, the  
235 barometric pressure is larger at these time periods and may result in stronger thermal coupling.  
236 The north-south seismic components experience larger diurnal tilt signals than the east-west  
237 components; it is possible that Pratas Island preferentially tilts north-south due to its east-west  
238 elongation (Figure 1c). It is possible that the preferential north-south tilt Pratas Island will bias  
239 transient tilt signals in the north-south direction.

#### 240 **4 Observations**

241 In order to find tilt signals on VDOS potentially generated by internal waves from the  
242 Luzon Strait we need to 1) identify transient tilt signals on VDOS, 2) compare the transient  
243 seismic tilt signals to established internal wave signals in satellite and oceanographic data, 3)  
244 verify that the tilt signals on VDOS are physical by comparing them to the temporary  
245 seismometers 6M75 and 6M88, and 4) determine whether tilt signals of interest are consistent  
246 with expected near-field tilt amplitudes generated by internal solitary waves in the South China  
247 Sea.

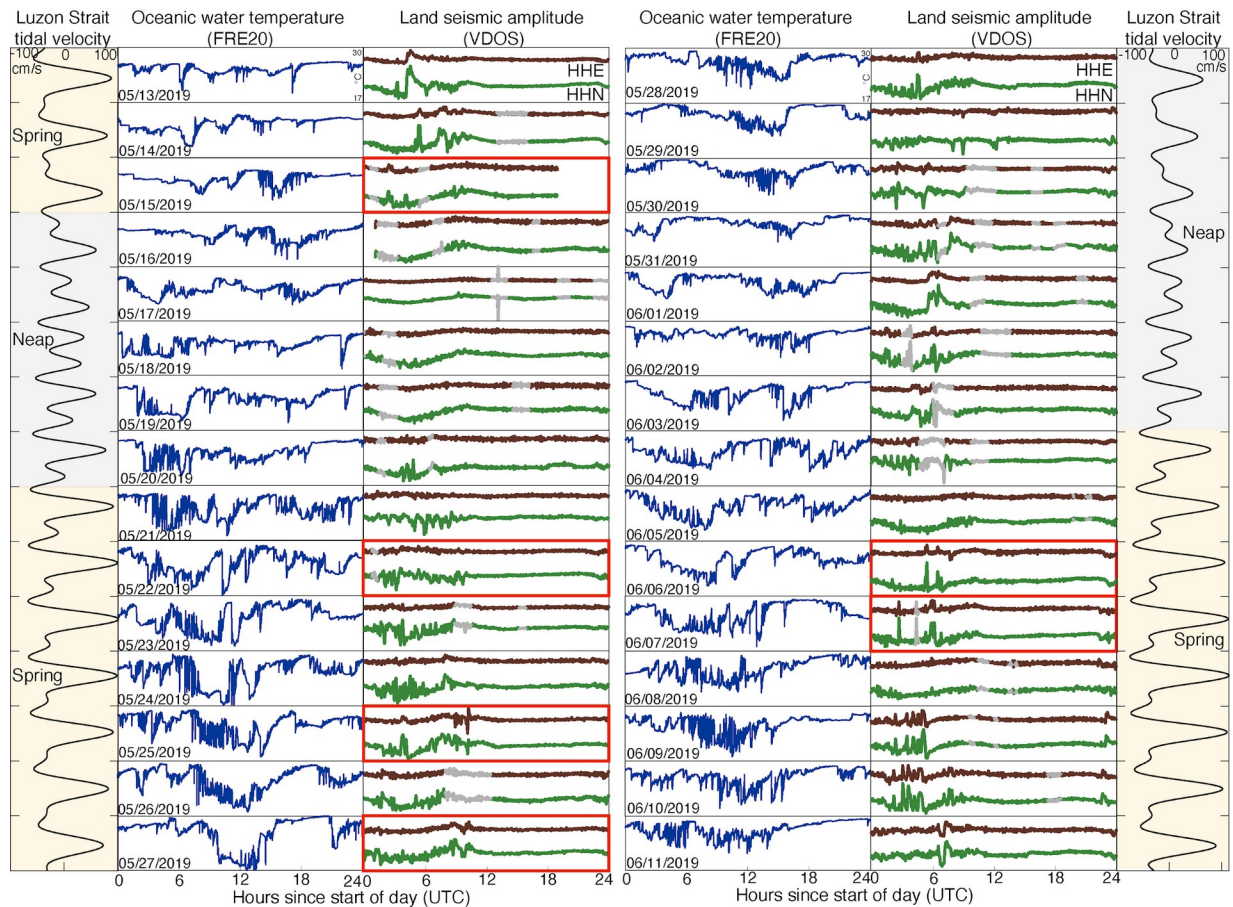
36  
37

38  
39

40  
248

#### 4.1 Transient seismic tilt signals

249 There are transient increases in tilt within the longer period diurnal noise on VDOS HHE  
250 and HHE (Figure 2). These signals appear to be largest and most frequent during spring tide at  
251 the Luzon Strait (Figure 2) when the largest amplitude internal waves are generated. Further,  
252 transient seismic tilt signals appear to increase at times when the oceanic temperature record at  
253 FRE20 has the highest variance, indicative of internal wave activity (Davis et al., 2008) (Figure  
254 2). It is therefore possible that some of the observed transient seismic tilt signals are due to  
255 internal waves arriving from the Luzon Strait. It should also be noted that the thermal transients  
256 on FRE20 are also due to non-tidal currents, the local internal tide, and locally-generated internal  
257 waves, which may also generate tilt observable on VDOS.



258

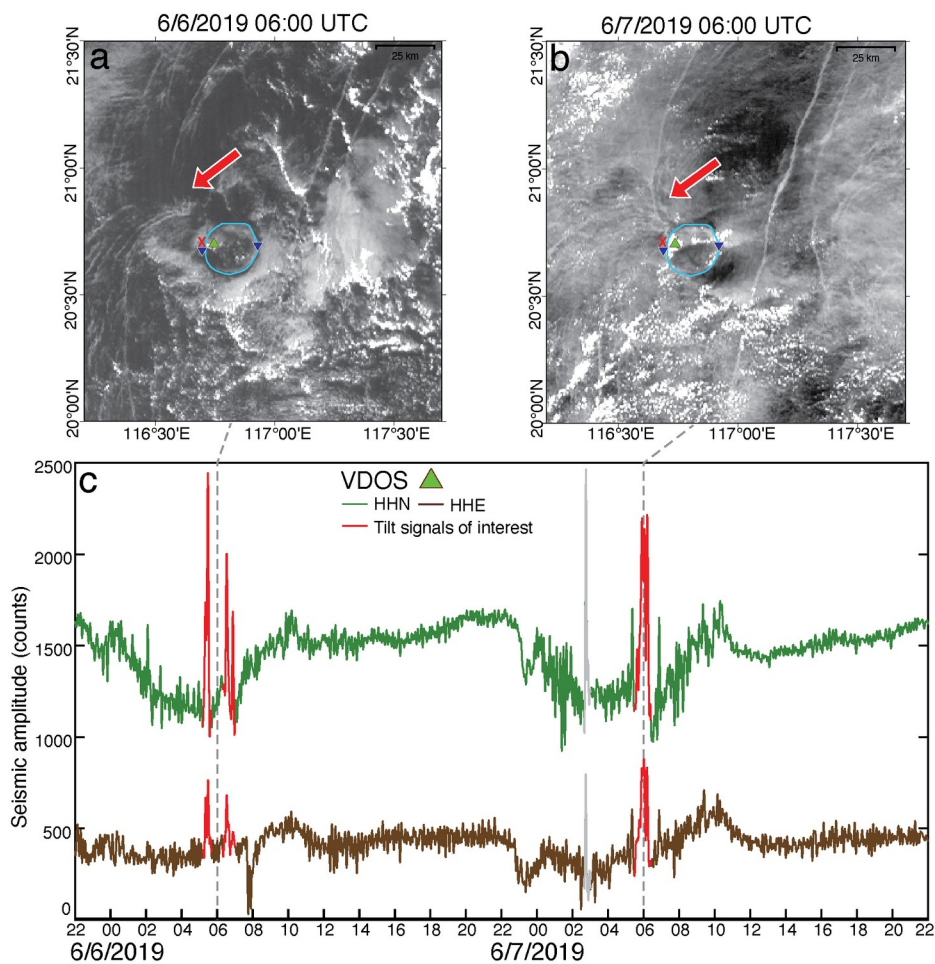
259 **Figure 2.** Oceanic water temperature and land seismic data from May 13 - June 11, 2019.  
260 Oceanic water temperature measurements at 19 m depth from FRE20 (Figure 1c) on the east side  
261 of Dongsha Atoll are shown in blue. VDOS HHE (brown) and HHN (green) components are  
262 shown with an acausal 400-second low-pass filter applied. Earthquake time periods are  
263 highlighted in grey. The Luzon Strait tidal velocities (black lines) were estimated using the  
264 Oregon State Tidal Inversion Software (Egbert and Erofeeva, 2002) and plotted with a 50-hour  
265 time shift. Spring (yellow) and neap (grey) time periods are indicated. The days that the seismic  
266 data is analyzed in more detail in sections 4.2-4.5 are highlighted in red.

41  
42

43  
4445  
267

## 4.2 Comparison of seismic and satellite observations

268 We use the Himawari-8 geostationary satellite images on exceptionally clear days from  
 269 June 6-7, 2019 (Figure 3a-c; Supporting Information Movie S1) to identify internal waves on the  
 270 western side of Dongsha Atoll for comparison to transient tilt signals on VDOS. We find that the  
 271 largest transient increases in tilt on VDOS HHN and HHE are temporally correlated with times  
 272 when internal waves are clearly visible on satellite images near the western side of Dongsha  
 273 Atoll near Pratas Island and VDOS (Figures 3c, 4i; Supporting Information Movie S1). The  
 274 potential seismic internal wave signals have durations of 30 minutes to 1 hour and are largest on  
 275 the HHN component (Figures 3c, 4i). There appear to be two seismic internal wave signals on  
 276 June 6 separated by one hour (Figure 3c). On June 7, there were two peaks in the transient tilt  
 277 signal (Figure 4i) but there is little separation.



278

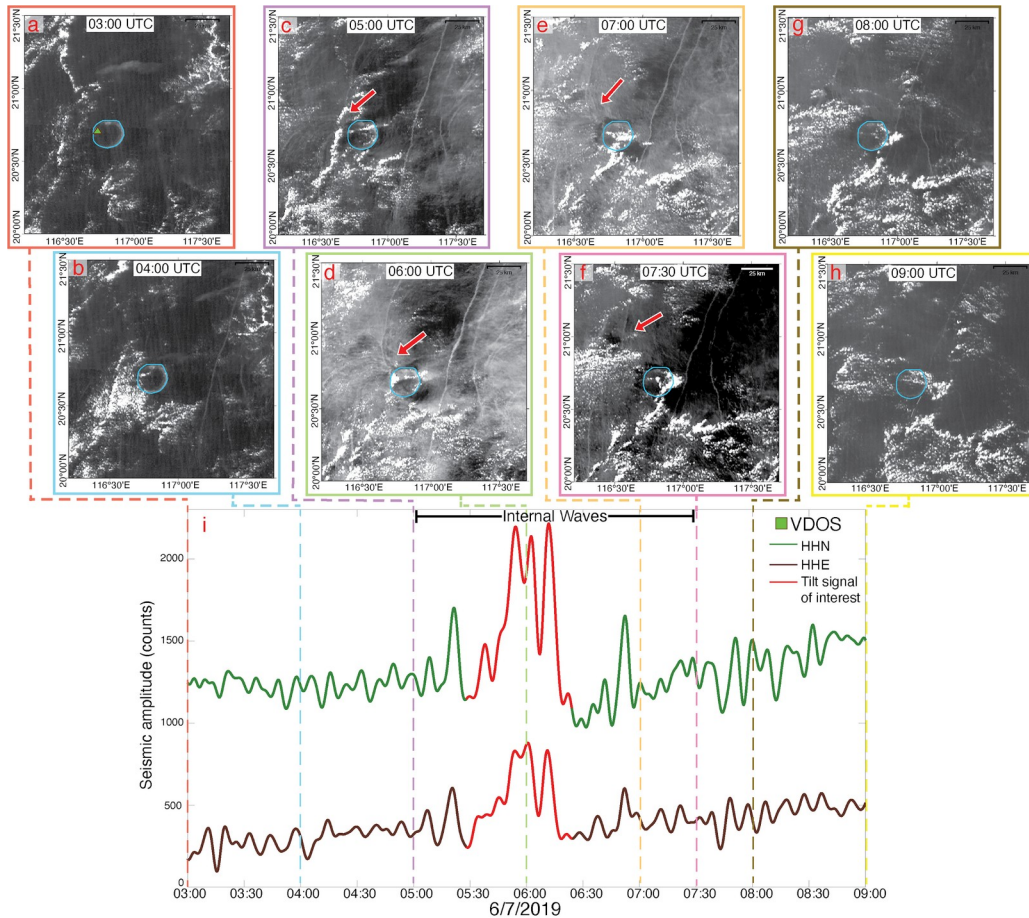
279 **Figure 3.** Comparison of satellite images and seismic observations as internal waves pass  
 280 Dongsha Atoll. (a)-(b) Himawari-8 standard red channel images on June 6, 2019 06:00 UTC and  
 281 June 7, 2019 06:00 UTC. Dongsha Atoll outlined in light blue. Seismic station VDOS on Pratas  
 282 Island (green triangle) and oceanic temperature sensors (blue inverted triangles) are included.  
 283 The closest point of internal waves to Pratas Island and VDOS is marked with a red X. Internal  
 284 waves passing around the western side of Dongsha Atoll are indicated by the red arrows. (c)  
 285 VDOS components HHE and HHN with an acausal 400-second low-pass filter applied. Tilt

46  
47

48  
49

50

286 signals potentially correlating with timing of internal wave arrivals on the western side of  
 287 Dongsha Atoll are indicated in red. Earthquake or instrument malfunction times are indicated in  
 288 grey. The timing of the satellite images are indicated by the dashed grey lines. Time is in UTC.  
 289 See Supporting Information Movie S1 for a movie of satellite images and seismic data from June  
 290 6 - June 7, 2019.



291

292 **Figure 4.** Detailed comparison of satellite images and seismic observations as internal waves  
 293 pass Dongsha Atoll. (a)-(h) Himawari-8 standard red channel images on June 7, 2019 from 03:00  
 294 - 09:00 UTC. Dongsha Atoll is outlined in light blue. VDOS seismic station is shown as the  
 295 green square on panel (a). Internal waves passing around the west side of Dongsha Atoll are  
 296 indicated by the red arrows. (i) VDOS components HHE and HHN with an acausal 400-second  
 297 low-pass filter applied. The largest tilt signal is highlighted in red. Timing of the satellite images  
 298 are indicated with dashed lines corresponding to the border colors of the satellite images. The  
 299 time period where internal waves are observed on the west side of Dongsha Atoll based on the  
 300 satellite images is indicated. Time is in UTC. See Supporting Information Movie S1 for a movie  
 301 of satellite images and seismic data from June 6 - June 7, 2019.

### 302 4.3 Comparison of seismic and oceanographic observations

303 There was significant cloud cover from May 18 - June 5, 2019 that prevented the  
 304 detection of internal waves on satellite images. We can therefore only compare transient seismic

51

52

10

53  
54

55

305 tilt signals to thermal transients indicative of internal waves in oceanic water temperature data  
306 during this time period. However, differentiating between internal waves arriving from the  
307 Luzon Strait, the local internal tide, and locally-generated internal waves at individual shallow  
308 oceanic temperature sensors is challenging, and all of these oceanic processes may generate tilt  
309 observable at VDOS. Further, depending on the depth of temperature measurements and the  
310 pycnocline, internal wave arrivals may be missed by individual shallow oceanic temperature  
311 sensors. We therefore rely on the deeper oceanic moorings located 6-9 km east of FRE20 before  
312 waves interact strongly with the bottom as a guide of expected arrival times for internal waves  
313 generated at the Luzon Strait.

314 Guided by the deeper moorings we were able to identify internal wave arrivals from the  
315 Luzon Strait on May 25 (Figure 5b) and May 27, 2019 (Figure 5a) during spring tide at both the  
316 shallow oceanic water temperature sensors (FRE20 and FRW15), with arrivals at FRW15  
317 lagging 2-4 hours behind FRE20. There are clear transient seismic tilt signals of similar duration  
318 on VDOS HHN and HHE that lag 1-1.5 hours behind FRW15 (Figure 5a-b). These lags are  
319 consistent with a packet of internal waves arriving at Dongsha Atoll from the Luzon Strait,  
320 breaking into northern and southern arms as they refract around the atoll, with the southern arm  
321 passing FRW15 before reaching the nearest point to VDOS. We were additionally able to  
322 identify internal wave arrivals at FRE20 on May 22, 2019 during spring tide (Figure 5c). An  
323 internal wave signal is not clear on FRW15 at the anticipated arrival time; however, there are  
324 transient tilt signals in the seismic data near the expected arrival time (Figure 5c).

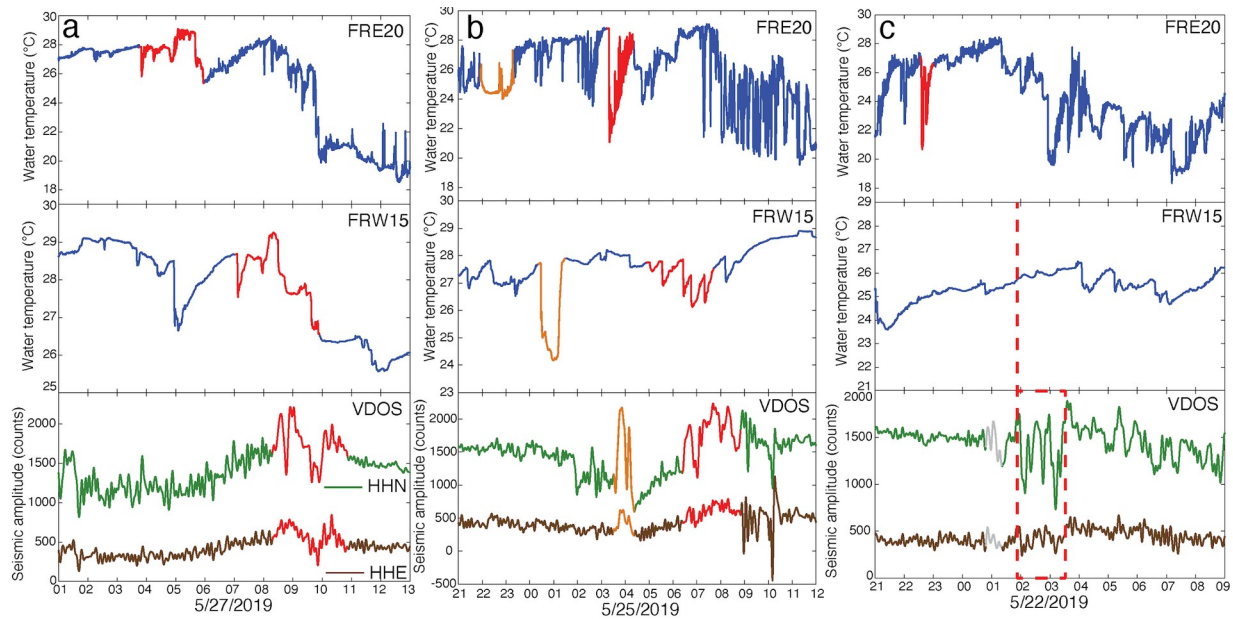
325 The thermal transient signals on FRE20 and FRW15 on May 25 and May 27 both related  
326 and potentially unrelated to internal wave activity warrant additional discussion. On May 27 the  
327 internal wave signal on FRW15 appears to occur during the local steepened internal tide. It is  
328 therefore possible that the observed seismic signal is from a combination of the internal wave  
329 arrival from the Luzon Strait and the local internal tide. Further, there was a temperature drop on  
330 FRW15 two hours prior to the internal wave arrival, which may also be related to the seismic  
331 signal (Figure 5a). On May 25 there was a large thermal transient propagating from FRE20 to  
332 FRW15 (highlighted in orange on Figure 5b) approximately 5 hours prior to the internal wave  
333 arrival from the Luzon Strait. There is also a transient tilt signal on VDOS that is lagged 3 hours  
334 behind FRW15. This lag is longer than the 1-1.5 hour lag observed for VDOS following FRW15  
335 for internal wave arrivals from the Luzon Strait (Figure 5a, b). This signal was not observed at  
336 the deeper offshore moorings and is therefore unlikely to arrive from the Luzon Strait. This  
337 transient may instead be a locally-generated internal wave. However, if this is an internal wave  
338 arrival from the Luzon Strait, the increased lag may be due to a collision point farther north of  
339 Pratas Island or a slower wave velocity.

56  
57

58

59

60



340

341 **Figure 5.** Comparison of shallow oceanic water temperature data to seismic observations at  
 342 VDOS during spring tide on May 27 (a), May 25 (b), and May 22 (c). Top: Shallow water  
 343 temperature measurements at 19 m depth (FRE20 on Figure 1c) on the east side of the Dongsha  
 344 Atoll shown in blue. Middle: Shallow water temperature measurements on the ocean bottom at  
 345 16.8 m depth (FRW15 on Figure 1c) on the west side of Dongsha Atoll shown in blue. Bottom:  
 346 VDOS components HHE (brown) and HHN (green) with an acausal 400-second low-pass filter  
 347 applied. Internal wave signals arriving from the Luzon Strait on shallow temperature data and  
 348 corresponding potential internal wave signals on VDOS are highlighted in red on (a) and (b). A  
 349 potential local internal wave signal is highlighted in orange in (b). The approximate timing of  
 350 internal wave arrivals on FRE20 is indicated by the red dashed line in (c) and a potential seismic  
 351 signal is indicated by the red dashed box. Time is in UTC.

61

62

12

63  
64

65

352

## 4.4 Signal across seismic stations

353

354

355

356

357

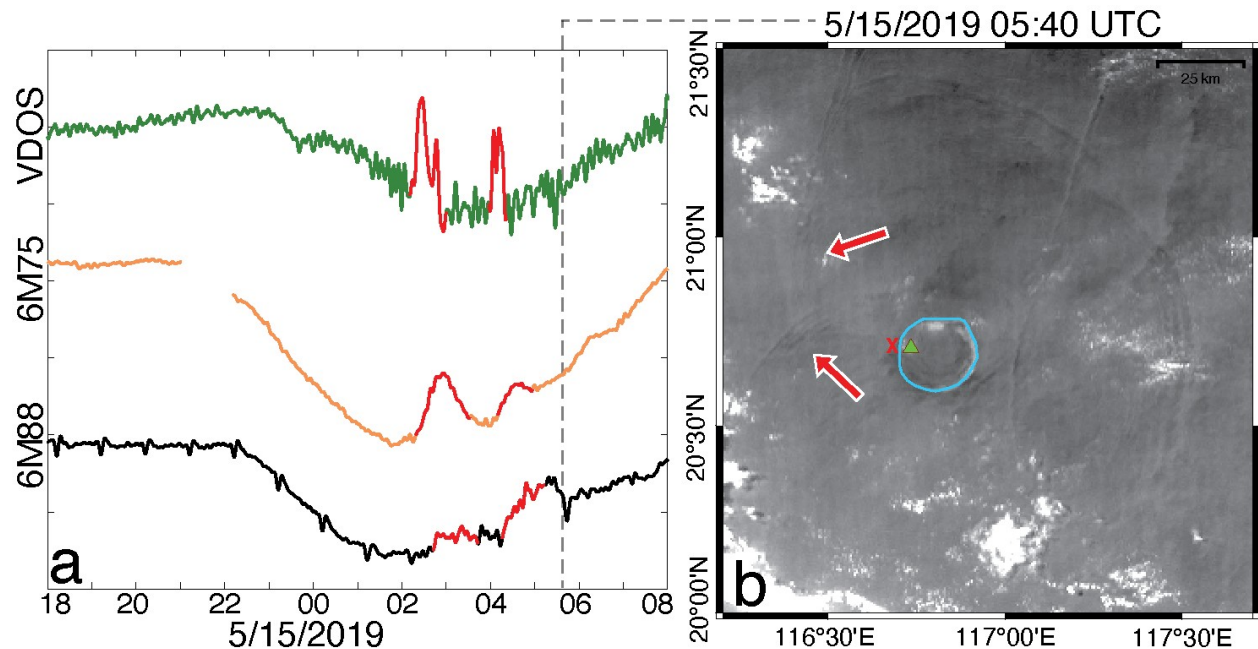
358

359

360

361

362



363

364

365

366

367

368

369

370

371

**Figure 6.** Comparison of tilt signal across seismic stations on May 15, 2019. (a) VDOS HHN (green), 6M75 BHN (orange), and 6M88 BHN (black) with acausal 400-second low-pass filters applied. Large transient tilt signals are highlighted in red. Timing of the satellite image in (b) is indicated by the grey dashed line. (b) Himawari-8 standard red channel images on May 15, 2019 at 05:40 UTC. Dongsha Atoll is outlined in blue. Seismic station VDOS on Pratas Island is indicated by the green triangle, the closest point of internal waves to Pratas Island and VDOS is marked with a red X. Internal waves that have recently passed Dongsha Atoll are indicated by the red arrows.

372

## 4.5 Seismic amplitude

373

374

375

376

377

We can estimate the seismic amplitudes during the six days of potential internal wave arrivals detailed in sections 4.1-4.4. We first deconvolve the instrument response to acceleration. We performed a simple linear detrend and then applied a cosine taper band-pass filter with four corner frequencies appropriate for identifying long-period tilt signals expected from internal waves (1/2400 Hz, 1/1200 Hz, 0.5 Hz, and 1 Hz). After the response was deconvolved we

66

67

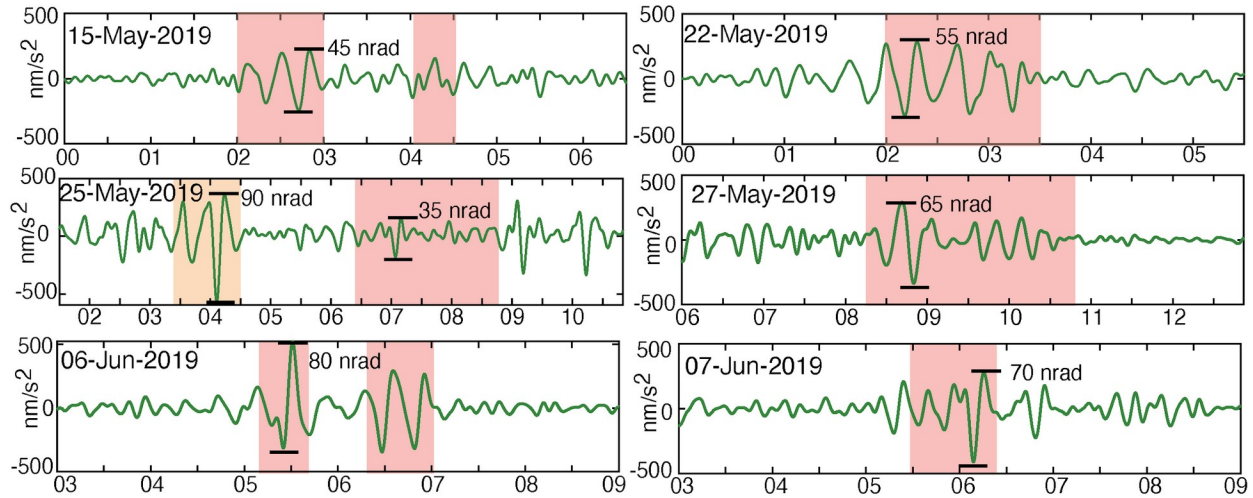
13

68

69

70

378 decimated the 100-Hz data to 1 Hz by downsampling by a factor of 10 twice, each time applying  
 379 a low-pass filter. We then applied an acausal 400-second low-pass filter to the seismic data and  
 380 analyzed the previously identified potential seismic internal wave signals in the raw seismic data  
 381 (Figure 7). It appears that peak seismic tilt signals range from roughly 35 to 80 nanoradians on  
 382 VDOS HHN (Figure 7). Tilt amplitudes are smaller for VDOS HHE, ranging from 15 to 35  
 383 nanoradians.



384

385 **Figure 7.** Amplitude of seismic internal wave detections. VDOS HHN (green) with the response  
 386 deconvolved and an acausal 400-second low-pass filter. Approximate timing of internal waves  
 387 near Pratas Island arriving from the Luzon Strait highlighted in red. A potential local internal  
 388 wave signal on May 25 highlighted in orange. Rough peak tilt amplitudes in nanoradians (nrad)  
 389 during internal wave time periods indicated in black. Timing (in hours) is UTC.

## 390 5 Summary of Observations and Potential Mechanisms

391 We have found promising evidence of the seismic detection of internal waves. First, there  
 392 are transient tilt signals on a permanent broadband seismometer onshore of Pratas Island that  
 393 appear to be larger and occur more frequently during spring tide when the largest amplitude  
 394 internal waves in the South China Sea are generated at the Luzon Strait (Figure 2). These are also  
 395 the time periods when the oceanographic temperature records have the highest variance,  
 396 indicative of internal wave activity (Davis et al., 2008). Second, we were able to temporally  
 397 correlate some of these transient seismic tilt signals with internal wave detections near Pratas  
 398 Island from satellite and oceanic water temperature measurements (Figures 3-6). Third, some of  
 399 the transient seismic tilt signals that correlate temporally with satellite and oceanographic  
 400 measurements are also observed on temporary seismometers on Pratas Island, indicating that  
 401 these tilt signals are physical (Figure 6). Finally, the seismic amplitude of the tilt signals of  
 402 interest are on the order of tens of nanoradians, consistent with expectations for a near-field  
 403 elastic tilt signal generated by internal solitary waves in the South China Sea (see Supporting  
 404 Information section S2 for calculation) (Figure 7). These observations taken together are strong  
 405 evidence of the seismic detection of internal waves.

406 We now consider two mechanisms to generate seismically observable transient tilt  
 407 signals through the pressure coupling of internal waves with the underlying seafloor.

71

14

72

73  
74

75

## 408 5.1 Passing of internal waves

409 The most straightforward mechanism for an internal wave to generate a seismically  
410 observable transient tilt signal is simply by passing near a broadband seismometer. As discussed  
411 in section 1, the hydrostatic pressure change and resulting elastic deformation of the underlying  
412 seafloor from a propagating internal solitary wave typical in the South China Sea would cause a  
413 near-field tilt of around 40 nanoradians (Figure 1d; Supporting Information section S2). This is a  
414 useful conceptual framework, though it is oversimplified for the geometry of Dongsha Atoll and  
415 requires further discussion.

416 Internal waves arriving from the Luzon Strait refract around Dongsha Atoll. Therefore,  
417 the nearest point internal waves reach to VDOS on Pratas Island is at the fore reef approximately  
418 4 km west of VDOS (marked on Figure 3a). It is anticipated that the largest hydrostatic pressure  
419 change and therefore near-field tilt signal observable by VDOS would occur at this point. This  
420 would generate a smaller tilt signal than expected from our calculation (Supporting Information  
421 section S2), which assumes the wave directly passes the seismometer. In addition, the waves are  
422 broken into a packet of elevation waves, rather than a single solitary wave of depression, which  
423 would further complicate the expected tilt signal.

424 It is worth noting that the two peaks in transient tilt observed on VDOS on June 6 (Figure  
425 3c) are consistent with the deeper mooring observation that this arrived as a two-packet wave.  
426 The June 7 wave was a single solitary wave and only one primary peak was observed in the  
427 seismic data (Figure 3c).

## 428 5.2 Collision of internal waves

429 Another mechanism for internal waves to generate seismically observable tilt signals is  
430 from wave-wave interactions or collisions that generate dynamic in addition to hydrostatic  
431 pressure changes. The northern and southern arms of internal wave trains collide after reaching  
432 the west side of Dongsha Atoll before eventually reforming (Figures 1b, 3a-b, 4c-f, Supporting  
433 Information Movie S1). These interactions would generate both dynamic and hydrostatic  
434 pressure changes coupled to the seafloor, causing near-field elastic displacement and tilt. We  
435 favor this mechanism for several reasons.

436 First, the observed tilt signals on the north-south component of VDOS range from 35-80  
437 nanoradians (Figure 7). This is larger than the 40 nanoradians expected from the hydrostatic  
438 pressure change alone, although it is still within the error of this simple calculation. Second, the  
439 seismic tilt signals lag 1-2 hours behind internal wave detections on the nearest oceanic  
440 temperature sensor (FRW15). The point of nearest approach to VDOS is roughly 3 km north of  
441 FRW15; we therefore expect internal waves to first be detected on FRW15. However,  
442 considering wave velocities ranging from 0.5-2 m/s, the seismic tilt signals are anticipated to lag  
443 25-100 minutes behind FRW15. The larger observed lag suggests that the peak seismic tilt  
444 signals are generated after the waves pass the nearest point to VDOS, potentially when the  
445 northern and southern arms interact. The seismic signal from wave-wave interactions may be  
446 from the collisions of multiple waves within a packet at the crossover point of the northern and  
447 southern arms. Based on satellite images during the study period (Figures 3a-b, 4c-f, Supporting  
448 Information Movie S1), these collisions occur north-northwest of Pratas Island, within the  
449 expected observational limit of VDOS of roughly 10 km.

76

15

77

80  
450 **6 Caveats and Conundrums**

## 451 6.1 North-south dominant tilt

452 The likely internal wave signals on VDOS are largest on the north-south component. This  
453 may be due to a combination of the preferential tilt of the island as well as the source of the tilt  
454 signals. It is likely that the east-west elongated Pratas Island preferentially tilts north-south, as is  
455 observed with the diurnal tilt signal (Figures 2, S1). It is unclear at this point if the preferential  
456 north-south tilt of Pratas Island would create a north-south bias for other transient tilt sources. In  
457 addition, internal waves “wrap” north-south around Dongsha Atoll (Li et al., 2013). When the  
458 northern and southern arms meet and collide on the west side of Dongsha Atoll, they are still  
459 propagating in a north-south direction (Figures 3a-b, 4c-f). This may produce a dominant north-  
460 south tilt. Further, the tilt experienced on Pratas Island may be amplified if this collision point  
461 occurs farther north or south, rather than due west of the island.

## 462 6.2 Detection of only one type of wave

463 During the study period all the potential internal wave signals identified in the seismic  
464 data occur between 02:00 and 11:00 UTC (10:00 and 19:00 local time). This is predominantly  
465 during daylight hours and within the large diurnal seismic tilt noise. No potential internal wave  
466 detections are made more than once per day. However, internal waves are generated up to twice  
467 daily at the Luzon Strait and have been classified as type-a or type-b waves (Duda et al., 2004;  
468 Ramp et al., 2004). Type-a waves are generated primarily by the K1 tide, typically have a large  
469 amplitude wave followed by smaller amplitude waves, and arrive at the same time each day, 24  
470 hours apart (Duda et al., 2004; Ramp et al., 2004). Type-b waves have a larger contribution from  
471 the M2 tidal constituent, propagate as a packet of waves, and arrive approximately one hour later  
472 each day (Duda et al., 2004; Ramp et al., 2004). Type-b waves are generated in the northern  
473 portion of the Luzon Strait while type-a waves are generated farther south (Du et al., 2008; Ramp  
474 et al., 2019). The deeper moorings provide more detailed observations of type-a and type-b  
475 waves during the deployment period. In general, type-a waves arrived as two or three-wave  
476 packets at an angle more south of east. Type-b waves arrived from almost due east as solitary  
477 waves that then broke into multi-wave packets of approximately equal amplitude and spacing  
478 between waves.

479 All of the potential seismic signals we identify are from type-b waves. During the study  
480 period, type-b waves arrive on the west side of Dongsha Atoll during daylight hours which  
481 allows for identification of these waves and wave-wave interactions on clear days near Pratas  
482 Island using satellite imagery. Type-a waves arrive at the east side of Dongsha Atoll around  
483 09:00 UTC (17:00 local time). We can therefore at times identify their arrival but cannot track  
484 these waves to the west side for better temporal comparison to onshore seismic data. This makes  
485 identifying a seismic signal from type-a waves difficult. Still, there are no clear transient tilt  
486 signals on VDOS during expected type-a arrival times on the west side of Dongsha Atoll. Below  
487 is a discussion of why type-a waves, and some type-b waves, may not be detected by VDOS.

488 The collision of the northern and southern arms refracting around Dongsha Atoll is likely  
489 a key generator of seismically observable tilt (see section 5.2). Therefore, refraction of waves  
490 around Dongsha Atoll and the location of the western collision are important for tilt generation.  
491 It is thus potentially significant that in this study only type-b waves have been observed to refract

83  
84

85

492 around Dongsha Atoll. This may be due to lack of satellite observations of type-a waves, or lack  
493 of satellite signature of type-a waves refracting.

494 Potential reasons for type-b waves to generate a seismically observable tilt while type-a  
495 waves do not include systematic differences in incoming angle, frequency content, depth of the  
496 main thermocline upon arrival during local internal tide, or interactions with the bottom. For  
497 instance, empirically it is seen that type-b waves refract asymmetrically around Dongsha Atoll  
498 resulting in the western collision occurring north-northwest of Pratas Island (Figures 3a-b, 4c-f,  
499 Supporting Information Movie S1). This may be due to the incoming angle, bathymetry and  
500 bathymetry-related velocity differences around the atoll. This asymmetry can generate a larger  
501 north-south pressure change and therefore north-south tilt of the underlying seafloor. Since the  
502 east-west elongated Pratas Island likely preferentially tilts north-south, this may be a more  
503 observable signal. Alternatively, type-a waves arrived with the local tide, creating more  
504 disturbances in the thermocline. Last and more speculatively, type-b waves may be affected by  
505 the bottom more than type-a waves (Ramp et al., in prep) perhaps due to their different frequency  
506 content, thus generating more of a pressure perturbation on the seafloor and therefore  
507 deformation and tilt. Type-a and type-b waves are generated in different parts of the Luzon Strait  
508 (Du et al., 2008; Ramp et al., 2019). This difference in generation site may affect the frequency  
509 content of the waves which may ultimately impact the interactions in the near-shore environment  
510 observed in the seismic data.

511 Not all type-b waves are clearly detected in the seismic data above the noise. The  
512 amplitude of waves will also determine the pressure change and near-field tilt signal. The diurnal  
513 tilt noise is around 5-10 nanoradians. Therefore, the tilt signal from a relatively small amplitude  
514 internal wave, potentially during neap tide, can likely be hidden in the diurnal tilt noise.

### 515 6.3 Seismic performance compared to existing methods

516 There are transient tilt signals on VDOS throughout the study period that we have not  
517 correlated with internal waves arriving from the Luzon Strait. This is partially due to incomplete  
518 satellite and oceanographic measurement coverage; however, it is likely that some of these  
519 signals are not from internal waves generated at the Luzon Strait. The local internal tide and  
520 locally-generated internal waves may also cause observable transient tilt signals on VDOS.  
521 Caution is therefore warranted at this time when identifying internal wave signals and their  
522 origin using seismic data alone.

523 Satellite imagery can provide remarkable spatial detail and identification of internal  
524 waves. However, satellite visible images are limited temporally, are unavailable at night and are  
525 highly unreliable during daylight hours. The deeper oceanic temperature moorings reliably detect  
526 internal waves of depression before they have interacted with the bottom and transformed, but  
527 are limited spatially. The shallow oceanic temperature sensors record internal waves after they  
528 have transformed into packets of elevation waves and are shoaling or breaking in the near-shore  
529 environment. The shallow temperature sensors are noisy, recording complicated near-shore  
530 internal wave interactions as well as non-tidal currents, the local internal tide, and locally-  
531 generated internal waves. Other measurements, such as satellite images or deeper moorings, are  
532 required to reliably identify internal waves arriving from the Luzon Strait in the shallow  
533 temperature data. The seismic data also requires additional verification of internal wave

86  
87

88  
89

90

534 identification at this time, but is currently performing similarly to the shallow temperature  
535 sensors.

#### 536 6.4 Mechanism

537 As discussed in section 5, the mechanism for internal waves to generate seismically  
538 observable tilt signals on Pratas Island is unclear. However, we favor large (i.e., observable by  
539 VDOS) transient tilt signals generated on the west side of Dongsha Atoll near Pratas Island as  
540 the northern and southern arms collide and reform, generating both hydrostatic and dynamic  
541 pressure changes on the underlying seafloor and therefore near-field tilt.

#### 542 7 Conclusion

543 It appears that we have successfully detected oceanic internal waves using a terrestrial  
544 island seismometer for the first time. We observe dominant north-south transient tilt signals on a  
545 broadband seismic station onshore of Pratas Island with amplitudes similar to what is expected  
546 from internal solitary waves arriving from the Luzon Strait. These seismic tilt signals appear  
547 correlated with internal wave detections in satellite and oceanic data, and apparently occur when  
548 waves collide nearshore. The north-south dominance is consistent with internal waves refracting  
549 around Dongsha Atoll and the east-west elongated Pratas Island preferentially tilting north-south.  
550 This initial detection suggests that the seismic detection and amplitude determination of oceanic  
551 internal waves is possible and can potentially be used to expand the historical record by  
552 capitalizing on the existing terrestrial seismic network.

#### 553 Acknowledgments, Samples, and Data

554 We are grateful for the support of Dongsha Atoll Research Station (DARS) and Dongsha Atoll  
555 Marine National Park. We are further grateful to Keryea Soong, Yi-Bei Liang, and Ke-Hsien Fu  
556 at National Sun Yat-sen University, Taiwan, and to Greg Sinnett and Sarah Merrigan, for their  
557 efforts in making this research possible. We are very grateful to Profs. Sen Jan, Y. J. Yang, and  
558 Ming-Huei Chang at National Taiwan University for the use of their deep mooring data for this  
559 study. The authors would also like to thank Thorne Lay for informative discussions that  
560 improved this work. K.A.D. was supported through funding provided by NSF-OCE 1753317.  
561 Maps were produced with the Generic Mapping Tools. Waveform data from the permanent  
562 seismic station used in this study (VDOS) is available at the Broadband Array in Taiwan for  
563 Seismology, Institute of Earth Sciences, Academia Sinica, Taiwan (doi: 10.7914/SN/TW).  
564 Waveform data from the temporary onshore deployment is archived at the Incorporated Research  
565 Institutions for Seismology Data Management Center (doi: 10.7914/SN/YD\_2019). Land  
566 temperature, humidity, and barometric pressure data from the temporary onshore deployment is  
567 archived at PANGEA (doi: In Progress). The shallow oceanic temperature data is archived at  
568 Dryad (doi: 10.7280/D1S39W). Satellite data is from the Himawari-8 geostationary  
569 meteorological satellite operated by the Japan Meteorological Agency (JMA).

#### 570 References

571 Ackerley, N., 2014, Principles of Broadband Seismometry, *in* Beer, M., Kougiumtzoglou, I.A.,  
572 Patelli, E., and Au, I.S.-K. eds., *Encyclopedia of Earthquake Engineering*, Berlin,  
573 Heidelberg, Springer Berlin Heidelberg, p. 1–35, doi:10.1007/978-3-642-36197-5\_172-1.

91

18

92

93  
94

95

- 574 Alford, M.H. et al., 2015, The formation and fate of internal waves in the South China Sea:  
575 *Nature*, v. 521, p. 65, doi:10.1038/nature14399.
- 576 Alpers, W., 1985, Theory of radar imaging of internal waves: *Nature*, v. 314, p. 245–247.
- 577 Anthony, R.E., Ringler, A.T., and Wilson, D.C., 2018, Improvements in Absolute Seismometer  
578 Sensitivity Calibration Using Local Earth Gravity Measurements Short Note: *Bulletin of*  
579 *the Seismological Society of America*, v. 108, p. 503–510, doi:10.1785/0120170218.
- 580 Arnosó, J., Viera, R., Velez, E., Weixin, C., Shiling, T., Jun, J., and Venedikov, A., 2001,  
581 Monitoring Tidal and Non-tidal Tilt Variations in Lanzarote Island (Spain): *Journal of the*  
582 *Geodetic Society of Japan*, v. 47, p. 456–462.
- 583 Bilham, R., and Beavan, J., 1979, Surface Deformation and Elasticity Studies in the Virgin  
584 Islands: National Aeronautics and Space Administration NSG 5072.
- 585 Davis, K.A., Arthur, R.S., Reid, E.C., Rogers, J.S., Fringer, O.B., DeCarlo, T.M., and Cohen,  
586 A.L., 2020, Fate of Internal Waves on a Shallow Shelf: *Journal of Geophysical Research:*  
587 *Oceans*, v. 125, p. e2019JC015377, doi:10.1029/2019JC015377.
- 588 Davis, K.A., Leichter, J.J., Hench, J.L., and Monismith, S.G., 2008, Effects of western boundary  
589 current dynamics on the internal wave field of the Southeast Florida shelf: *Journal of*  
590 *Geophysical Research: Oceans*, v. 113, doi:https://doi.org/10.1029/2007JC004699.
- 591 DeCarlo, T.M., Karnauskas, K.B., Davis, K.A., and Wong, G.T.F., 2015, Climate modulates  
592 internal wave activity in the Northern South China Sea: *Geophysical Research Letters*, v.  
593 42, p. 2014GL062522, doi:10.1002/2014GL062522.
- 594 Du, T., Tseng, Y.-H., and Yan, X.-H., 2008, Impacts of tidal currents and Kuroshio intrusion on  
595 the generation of nonlinear internal waves in Luzon Strait: *Journal of Geophysical*  
596 *Research: Oceans*, v. 113, doi:https://doi.org/10.1029/2007JC004294.
- 597 Duda, T.F., Lynch, J.F., Irish, J.D., Beardsley, R.C., Ramp, S.R., Chiu, C.-S., Tang, T.Y., and  
598 Yang, Y.-, 2004, Internal tide and nonlinear internal wave behavior at the continental  
599 slope in the northern south China Sea: *IEEE Journal of Oceanic Engineering*, v. 29, p.  
600 1105–1130, doi:10.1109/JOE.2004.836998.
- 601 Egbert, G.D., and Erofeeva, S.Y., 2002, Efficient Inverse Modeling of Barotropic Ocean Tides:  
602 *Journal of Atmospheric and Oceanic Technology*, v. 19, p. 183–204, doi:10.1175/1520-  
603 0426(2002)019<0183:EIMOBO>2.0.CO;2.
- 604 Ekström, G., Dalton, C.A., and Nettles, M., 2006, Observations of Time-dependent Errors in  
605 Long-period Instrument Gain at Global Seismic Stations: *Seismological Research Letters*,  
606 v. 77, p. 12–22, doi:10.1785/gssrl.77.1.12.
- 607 Ferrari, R., and Wunsch, C., 2009, Ocean Circulation Kinetic Energy: Reservoirs, Sources, and  
608 Sinks: *Annual Review of Fluid Mechanics*, v. 41, p. 253–282,  
609 doi:10.1146/annurev.fluid.40.111406.102139.
- 610 Fu, K.-H., Wang, Y.-H., St. Laurent, L., Simmons, H., and Wang, D.-P., 2012, Shoaling of large-  
611 amplitude nonlinear internal waves at Dongsha Atoll in the northern South China Sea:  
612 *Continental Shelf Research*, v. 37, p. 1–7, doi:10.1016/j.csr.2012.01.010.
- 613 Garrett, C., and Kunze, E., 2007, Internal Tide Generation in the Deep Ocean: *Annual Review of*  
614 *Fluid Mechanics*, v. 39, p. 57–87, doi:10.1146/annurev.fluid.39.050905.110227.
- 615 Helfrich, K.R., and Melville, W.K., 2006, Long Nonlinear Internal Waves: *Annual Review of*  
616 *Fluid Mechanics*, v. 38, p. 395–425, doi:10.1146/annurev.fluid.38.050304.092129.

96  
97

19

100

617 Holloway, P.E., Pelinovsky, E., Talipova, T., and Barnes, B., 1997, A Nonlinear Model of  
618 Internal Tide Transformation on the Australian North West Shelf: *JOURNAL OF*  
619 *PHYSICAL OCEANOGRAPHY*, v. 27, p. 26.

620 Jackson, C., da Silva, J., Jeans, G., Alpers, W., and Caruso, M., 2013, Nonlinear Internal Waves  
621 in Synthetic Aperture Radar Imagery: *Oceanography*, v. 26,  
622 doi:10.5670/oceanog.2013.32.

623 Li, X., Jackson, C.R., and Pichel, W.G., 2013, Internal solitary wave refraction at Dongsha Atoll,  
624 South China Sea: *Geophysical Research Letters*, v. 40, p. 3128–3132,  
625 doi:10.1002/grl.50614.

626 Lien, R.-C., Tang, T.Y., Chang, M.H., and D'Asaro, E.A., 2005, Energy of nonlinear internal  
627 waves in the South China Sea: *Geophysical Research Letters*, v. 32,  
628 doi:10.1029/2004GL022012.

629 MacKinnon, J.A. et al., 2017, Climate Process Team on Internal Wave–Driven Ocean Mixing:  
630 *Bulletin of the American Meteorological Society*, v. 98, p. 2429–2454,  
631 doi:10.1175/BAMS-D-16-0030.1.

632 Miropol'sky, Y.Z., 2001, *Dynamics of Internal Gravity Waves in the Ocean* (O. D. Shishkina,  
633 Ed.): Springer Netherlands, Atmospheric and Oceanographic Sciences Library,  
634 <https://www.springer.com/us/book/9780792369356> (accessed February 2019).

635 Moun, J.N., and Smyth, W.D., 2006, The pressure disturbance of a nonlinear internal wave  
636 train: *Journal of Fluid Mechanics*, v. 558, p. 153, doi:10.1017/S0022112006000036.

637 Ramp, S.R., Park, J.-H., Yang, Y.J., Bahr, F.L., and Jeon, C., 2019, Latitudinal Structure of  
638 Solitons in the South China Sea: *Journal of Physical Oceanography*, v. 49, p. 1747–1767,  
639 doi:10.1175/JPO-D-18-0071.1.

640 Ramp, S.R., Tang, T.Y., Duda, T.F., Lynch, J.F., Liu, A.K., Chiu, C.-S., Bahr, F.L., Kim, H.-R.,  
641 and Yang, Y.-, 2004, Internal solitons in the northeastern south China Sea. Part I: sources  
642 and deep water propagation: *IEEE Journal of Oceanic Engineering*, v. 29, p. 1157–1181,  
643 doi:10.1109/JOE.2004.840839.

644 Ramp, S.R., Yang, Y.J., and Bahr, F.L., 2010, Characterizing the nonlinear internal wave climate  
645 in the northeastern South China Sea: *Nonlinear Processes in Geophysics*, v. 17, p. 481–  
646 498, doi:10.5194/npg-17-481-2010.

647 Ramp, S.R., Yang, Y.-J., Jan, S., Chang, M. -H, Davis, K. A., Sinnett, G., Bahr, F. L., Reeder, D.  
648 B., and Ko, D. S., in prep, From the Basin to the Beach: Shoaling Solitons on an Isolated  
649 Tropical Reef.

650 Ray, R.D., and Mitchum, G.T., 1996, Surface manifestation of internal tides generated near  
651 Hawaii: *Geophysical Research Letters*, v. 23, p. 2101–2104, doi:10.1029/96GL02050.

652 Reid, E.C., DeCarlo, T.M., Cohen, A.L., Wong, G.T.F., Lentz, S.J., Safaie, A., Hall, A., and  
653 Davis, K.A., 2019, Internal waves influence the thermal and nutrient environment on a  
654 shallow coral reef: *Limnology and Oceanography*, v. 64, p. 1949–1965,  
655 doi:<https://doi.org/10.1002/lno.11162>.

656 Rogers, J.S., Rayson, M.D., Ko, D.S., Winters, K.B., and Fringer, O.B., 2019, A framework for  
657 seamless one-way nesting of internal wave-resolving ocean models: *Ocean Modelling*, v.  
658 143, p. 101462, doi:10.1016/j.ocemod.2019.101462.

659 Sandstrom, H., and Elliott, J.A., 1984, Internal tide and solitons on the Scotian Shelf: A nutrient  
660 pump at work: *Journal of Geophysical Research: Oceans*, v. 89, p. 6415–6426,  
661 doi:10.1029/JC089iC04p06415.

101

20

102

103  
104

105

- 662 Simmons, H., Chang, M.-H., Chang, Y.-T., Chao, S.-Y., Fringer, O., Jackson, C., and Ko, D.S.,  
663 2011, Modeling and Prediction of Internal Waves in the South China Sea: *Oceanography*,  
664 v. 24, p. 88–99, doi:10.5670/oceanog.2011.97.
- 665 Wang, Y.-H., Dai, C.-F., and Chen, Y.-Y., 2007, Physical and ecological processes of internal  
666 waves on an isolated reef ecosystem in the South China Sea: *Geophysical Research*  
667 *Letters*, v. 34, doi:<https://doi.org/10.1029/2007GL030658>.
- 668 Wielandt, E., and Forbriger, T., 1999, Near-field seismic displacement and tilt associated with  
669 the explosive activity of Stromboli: *Annals of Geophysics*, v. 42, doi:10.4401/ag-3723.
- 670 Wolanski, E., and Deleersnijder, E., 1998, Island-generated internal waves at Scott Reef,  
671 Western Australia: *Continental Shelf Research*, v. 18, p. 1649–1666, doi:10.1016/S0278-  
672 4343(98)00069-7.
- 673 Woodson, C.B., 2018, The Fate and Impact of Internal Waves in Nearshore Ecosystems: *Annual*  
674 *Review of Marine Science*, v. 10, p. 421–441, doi:10.1146/annurev-marine-121916-  
675 063619.
- 676 Zhao, Z., Klemas, V., Zheng, Q., and Yan, X.-H., 2004, Remote sensing evidence for baroclinic  
677 tide origin of internal solitary waves in the northeastern South China Sea: *Geophysical*  
678 *Research Letters*, v. 31, doi:10.1029/2003GL019077.
- 679

106

107

21